Journal of Climate Change
ISSN 2395-7611 Volume 12 (2026) No. 1. pp. 106–127

https://doi.org/10.70917/jcc-2026-007

Article

Composition-Resolved Spectral Absorption and Thermal Heating Effects of Dust Layers on Crystalline Silicon Photovoltaic Modules

Kudzanayi Chiteka [1,*] and C.C. Enweremadu [1]

[1] Department of Mechanical, Bioresources and Biomedical Engineering, University of South Africa, Science Campus, Florida 1710, South Africa
* Correspondence author: echitekk@unisa.ac.za

Abstract: Dust deposition on photovoltaic modules induces losses through wavelength-selective attenuation and dust-driven heating, but most soiling models quantify only optical transmission. The present study developed a composition-resolved optical-thermal framework that links measured dust mineralogy to coupled spectral and temperature-dependent power degradation in crystalline silicon modules. Dust was collected from operating PV modules in Harare (Zimbabwe) and Roodepoort (South Africa) and characterized for particle size, mass loading, and oxide composition. Oxide fractions were converted to effective complex refractive indices using an effective-medium formulation, and Mie-based calculations were used to compute spectral absorptance in the range 400-900 nm. The absorbed radiative flux was then introduced as a heat-input term in a surface energy-balance model to predict dust-induced cell-temperature rise, and the modified spectrum and temperature were propagated to electrical metrics. At a representative loading of 2.0 g/m^2, the model predicted a temperature rise of 4.8 °C for Roodepoort dust and 4.6 °C for Harare dust. The corresponding total power losses were 14.2% and 13.8%, respectively. Solar simulator validation showed measured temperature rises of 4.52 °C and 4.29 °C for Roodepoort and Harare dust, giving deviations of 5.73% and 6.81% from the model predictions. Using the measured temperature rises and a crystalline silicon temperature coefficient of 0.45%/°C, the temperature-aligned total power losses were estimated as 14.08% and 13.66% for Roodepoort and Harare dust, respectively. These results confirm that dust induced heating amplifies optical soiling losses and should be included when forecasting yield and defining cleaning triggers in dusty, high irradiance environments.

Keywords: Spectral soiling; Dust composition; Optical-thermal modelling; Crystalline silicon photovoltaics; Performance degradation; Dust absorptance.

1. Introduction

The global energy sector is undergoing a fundamental transformation aimed at reducing carbon emissions and mitigating the increasingly destructive effects of climate change. Among the available renewable energy sources, photovoltaic systems stand out as one of the most scalable and widely utilized technologies for converting sunlight into electricity, offering a critical solution to meet the growing global energy demand while addressing environmental concerns (Riffat and Samaei, 2025; Sovetova et al., 2025). However, photovoltaic systems are affected by soiling through the accumulation of dust, soot, and organic debris on the solar PV module surface. This contamination can reduce power output by as much as 40% depending on deposition rate, particle type, cleaning frequency, and prevailing environmental conditions (Pelland et al., 2018). Global assessments indicate that soiling rates typically range from about 0.5% to above 6% per month, with arid and semi-arid regions being especially vulnerable because rainfall-driven natural cleaning is limited and deposited material persists for longer periods (Pelland et al., 2018; Tsanakas et al., 2025). Long-term field observations also show strong site dependence, where multi-year measurements in Qatar, for instance, reported seasonal variability in soiling intensity and dust storms increased annual soiling levels by about 23% due to shifts in rainfall and wind-driven resuspension (Javed et al., 2020). Similar trends were observed in Arizona, where power losses of 3.8 - 11.1% were linked to installation configuration and proximity to urban dust sources (Mallineni et al., 2014). Monitoring in Oman, supported by more than 36 000 environmental datapoints, further confirmed that dust accumulation and PV performance respond dynamically to temperature, humidity, and land-use patterns (Al Humairi et al., 2024).

The characteristics of deposited dust govern the magnitude of performance degradation. Fine particles (<45 µm) reduce light transmission more severely than coarse particles because they pack more densely and reduce optical pathways through the soiling layer (Sisodia, 2024). Comparative site investigations in Egypt and Jordan further revealed that dark and fine dust produces sharper transmission losses and greater thermal loading even when mass loading is similar (Øvrum et al., 2021). Laboratory studies support these trends by showing that reduced inter-particle void space increases attenuation, and that iron-rich dust increases solar absorption through low albedo and enhanced scattering behaviour (Riaz and Mahmood, 2022). Field measurements in Senegal indicate that even limited iron chloride and carbon-based minerals can reduce reflectance by up to 30%, altering spectral transmittance and thermal gain (Drame et al., 2021). Spectral observations from desert PV installations in China further indicate stronger attenuation at shorter wavelengths for smaller and darker particles, demonstrating that soiling losses depend on optical and physical properties as well as deposited mass (Zhang et al., 2024).

The optical behaviour of a soiled PV surface is controlled by transmittance, reflectance, and absorptance, which depend on dust morphology, surface coverage, particle size, packing density, and refractive index (Kaneria and Reddy, 2025; Mandal and Reddy, 2025). These properties determine whether incoming radiation is transmitted to the cell, reflected away, or absorbed within the dust layer. Therefore, deposition density and uneven accumulation can increase localised shading and attenuation (Razak et al., 2026), while the complex refractive index governs light propagation and absorption, especially in iron oxide and carbonaceous phases (Kutlu et al., 2025). Experimental observations show that dust accumulation on solar glass reduces transmittance as scattering and absorption increase with deposition (Abdellatif et al., 2023). Modelling studies further indicate that when dust-layer thickness approaches or exceeds the characteristic particle diameter, light propagation becomes strongly inhibited and transmission can decrease sharply, particularly for fine mineral dust (Xu et al., 2020). Measurements under Saharan dust exposure show that a layer thickness of about 70 µm, equivalent to approximately 3.3 g/m², can reduce visible transmittance by more than half, with only about 48% of incident radiation reaching the cell surface (Diop et al., 2020).

Particle shape and dust spatial distribution also contribute to the optical response, since irregular and porous particles enhance forward scattering and increase effective optical path length, while dense packing and angular grains modify scattering directionality (Tanesab et al., 2019). Non-uniform deposition can also generate localised shading and uneven optical attenuation across the module surface (ul Haq et al., 2024). A three-layer optical model involving the dust layer, glass cover, and solar cell further confirms that particle-size heterogeneity and layer thickness dominate spectral transmittance within the crystalline silicon response window of 350 to 1000 nm. This effect is strongest in the visible band of 350 to 700 nm, where dust-induced scattering and absorption distort the spectrum (Susa et al., 1992; Xu et al., 2020).

Absorptivity and complex refractive index are therefore central in determining whether incoming light is scattered or absorbed at the module surface. Dust containing iron oxides or carbon-rich material absorbs visible radiation more effectively than silica-based particles and exhibits lower reflectance and higher absorptivity, leading to stronger optical losses and increased surface temperature (Rezvani et al., 2023; Tanesab et al., 2019; Willers et al., 2025). Field measurements show that the imaginary component of the complex refractive index strongly controls absorption across the solar spectrum, and mineral-to-mineral variability can significantly alter spectral behaviour (Yus-Díez et al., 2025). Similar temperature and power impacts have been reported near cement production sites where elevated iron oxide content increased module temperature and lowered output (Riaz and Mahmood, 2022). Studies comparing absorbing and non-absorbing dust further show that transmission decreases approximately linearly with increasing dust mass, with a steeper decline for carbonaceous and iron-bearing phases (Darwish et al., 2021; Piedra et al., 2018). This is consistent with radiative-transfer simulations and analytical optical models indicating larger extinction cross sections and stronger wavelength-dependent attenuation for darker particles (Boyle et al., 2015; Piedra et al., 2018). Soiling also alters the spectral distribution reaching the cell, where selective attenuation of shorter wavelengths reduces current generation beyond what is inferred from single-value transmission metrics (Fernández-Solas et al., 2022; Micheli et al., 2019). Optical measurements and field evaluations confirm that refractive index and absorptivity control this response and that spectral distortion contributes to current mismatch and efficiency decline when absorbing phases are present (Fernández et al., 2019; John et al., 2015; Smestad et al., 2020). Concentrator and multi-junction systems exhibit related sensitivity because short-wavelength losses influence current balance among subcells (Fernández et al., 2019), and measurements on silicon photodiodes indicate that spectral response varies with incidence angle due to reflectance changes, emphasizing combined effects of dust composition, optical geometry, and illumination angle (Boivin, 2001).

Soiling losses are often estimated using empirical models based on historical performance and cleaning intervals, but these models do not generalize well across climates because particle composition, environmental variability, and deposition dynamics are not represented (Pagani et al., 2021). Comparative evaluations show that regression-based approaches can yield errors of about 40% to above 90% when transient effects such as wind and light precipitation are not captured (Sharma et al., 2023). Long-term forecasting also indicates that treating soiling as static can shift energy-yield predictions by more than 10% (Muller and Rashed, 2023). Physics-based approaches instead represent scattering and absorption explicitly, where Mie theory enables estimation of optical losses using particle size and refractive index and has been applied to concentrating solar power and PV systems (Bellmann et al., 2020). Furthermore, two-stream radiative-transfer models provide structured representations for layered scattering and absorption (Lu et al., 2009). Parameterisations incorporating deposition velocity and microphysical properties improve accuracy relative to empirical baselines (Lara-Fanego et al., 2023), yet cross-plant comparisons show that oversimplified formulations can still produce high RMSE in large-scale operation (Redondo et al., 2024). These findings indicate that reliable prediction requires models that represent dust optical properties together with environmental processes that govern accumulation and removal.

Electrical performance of crystalline silicon modules is also strongly temperature dependent. As cell temperature increases, open-circuit voltage decreases and conversion efficiency declines, with typical temperature coefficients of -0.3 to -0.5% /°C depending on design and material quality (Perin Gasparin et al., 2022). Simulations show that increasing ambient temperature from 25 to 50 °C reduces efficiency even at constant irradiance, emphasizing the importance of thermal regulation (Muhfidin and Yu, 2019). Module temperature is set by radiative, convective, and conductive heat-transfer processes that depend on wind, air temperature, and mounting configuration (Gómez, 2009; Rosli et al., 2014). Heat-transfer modelling shows sensitivity to tilt and airflow, while multiphysics simulations under desert conditions confirm that elevation and improved ventilation can lower operating temperature and reduce performance losses (Hassanian et al., 2022; Limane et al., 2023). High-resolution modelling further indicates that temperature can vary spatially across a module surface, producing localized electrical-performance variations even under uniform irradiance (Tomšič et al., 2025).

Although optical and thermal effects of soiling are often treated separately, their combined influence remains insufficiently represented in PV performance models. Dust is frequently modelled only as an optical attenuator, which neglects additional heating when absorbing particles increase surface temperature and leads to underestimation of losses in environments with carbonaceous or iron-bearing minerals (Gu et al., 2023; Zarei and Abdolzadeh, 2016). Recent attempts to link optical and thermal behaviour typically do not incorporate mineralogical composition and particle-size effects systematically and therefore cannot resolve composition-dependent spectral and thermal consequences (Gu et al., 2023; Hoang et al., 2014). Other studies have emphasised Mie-based scattering analysis without accounting for heat accumulation at the module surface (Bellmann et al., 2020). Observations from naturally soiled modules also indicate that short-wavelength attenuation is accompanied by increased temperature, but the coupled impacts on current and voltage have not been quantified in a composition-sensitive framework (Smestad et al., 2020).

Despite this progress, literature still treats the optical and thermal effects of soiling mainly as separate problems. Qaisieh et al., (2023) quantified the optical transmission losses caused by dust accumulation and showed how these losses reduce the irradiance reaching the PV surface. Abdellatif et al., (2023) also used Mie theory to model optical scattering, transmittance, and absorptance through dust layers on PV surfaces. However, these optical-based approaches do not fully account for dust-induced heating and the related temperature-driven electrical degradation. As a result, they may underestimate performance loss when dust contains strongly absorbing mineral or carbonaceous phases. Therefore, composition-resolved models that connect mineralogy, spectral attenuation, dust heating, and electrical response remain limited. To address this gap, the present study developed a composition-resolved coupled optical-thermal framework that links measured dust mineralogy and particle-size properties to wavelength-dependent optical losses, dust-induced cell-temperature rise, and thermally amplified electrical degradation in crystalline silicon PV solar cells. This framework goes beyond conventional optical-only approaches by explicitly accounting for thermal amplification driven by dust composition, thereby providing a clearer basis for operational decisions such as cleaning prioritisation under absorber-rich, high-irradiance, low-wind, and high-temperature conditions. This paper is organized as follows: the methodology describes the composition-resolved optical modelling, refractive-index derivation, and coupled energy-balance formulation, the results quantify spectral and thermal contributions across dust types and loadings, and this is followed by the conclusion and future directions section.

2. Methodology

The present study applied a composition-resolved optical-thermal modelling framework to quantify how dust mineralogy influences wavelength-dependent transmission losses and thermally induced performance degradation in crystalline silicon photovoltaic modules. The analysis was grounded on field-collected dust samples obtained from two different urban environments, thereby enabling comparative assessment of composition-driven soiling impacts under different geographic and environmental conditions.

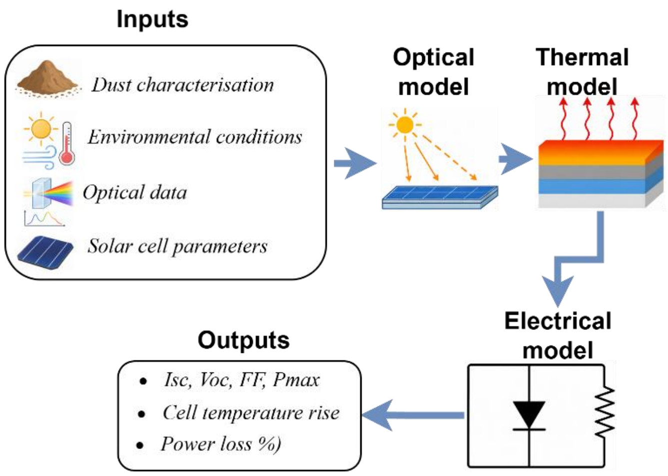

Figure 1. Workflow of the coupled optical, thermal, and electrical PV model showing the progression from inputs to model outputs.

Figure 1 illustrates the coupled optical, thermal, and electrical workflow of the model. The inputs, comprising dust characterisation, environmental conditions, optical data, and PV module parameters, were first processed in the optical model to determine spectral transmittance, reflectance, and absorptance. These outputs were then propagated to the thermal model, where absorbed radiation and transmitted irradiance were used to compute the cell temperature, accounting for convective, radiative, and conductive heat transfer. The computed temperature was subsequently used in the electrical model to determine short-circuit current, open-circuit voltage, fill factor, and maximum power, producing the final performance metrics. The figure further emphasizes the coupling between the thermal and electrical models, thereby providing a clear visual summary of the flow of information from measured dust properties to predicted PV module performance.

2.1. Dust sampling and characterisation

Dust sampling was conducted in Harare, Zimbabwe (17.8252°S, 31.0335°E), and Roodepoort, South Africa (26.1625°S, 27.8725°E). Harare is characterized by a subtropical climate with a distinct dry season and frequent urban dust activity linked to traffic and construction, while Roodepoort lies on a highland and is influenced by periodic wind events, traffic and industrial particulate sources. Dust was obtained directly from the surfaces of operating PV modules during dry, stable atmospheric conditions to minimize moisture-related interference and to preserve the natural adhesion state of the deposited layer. A clean, non-abrasive micro-spatula was used to lift surface dust, and the collected material was transferred into airtight containers to limit contamination and particle loss during storage and transport.

Dust samples were air-dried under controlled temperature and humidity to remove residual moisture without altering particle morphology, porosity, or surface structure, which could affect optical and thermal behavior. Surface mass loading was measured gravimetrically by recording the mass difference of pre-cleaned glass substrates before and after dust application using a high-precision microbalance. This measurement provided the areal density (g/m^2) of dust, which is a critical input for both optical and thermal modeling. Particle-size distributions were obtained from scanning electron microscopy images, followed by quantitative granulometric analysis in ImageJ. From these images, the median particle radius, geometric standard deviation, and size percentiles (10%, 50%, 90%) were extracted, providing detailed information on dust fineness and spread across the module surface.

Elemental composition was determined using energy-dispersive X-ray spectroscopy (EDS) and measured elemental mass fractions were converted to corresponding oxide forms to represent mineralogical content. Dust mineralogy is strongly region-specific. Therefore, the Harare and Roodepoort samples were treated as separate site-specific dust populations rather than as a universal dust composition. This was necessary since variations in soil type, traffic emissions, construction activity, industrial particles, weather conditions, and natural mineral sources can alter the abundance of silica, aluminosilicates, iron oxides, carbonaceous materials, and other absorbing phases. Thus, the EDS-derived oxide fractions were used to preserve the measured regional compositional differences before estimating the effective optical properties.

All sample handling was performed carefully without grinding or chemical processing to preserve the native morphology of particles, ensuring that the dust properties used in the model reflect realistic field conditions. The resulting dataset for each location included areal mass loading, particle-size metrics, effective density, and oxide composition. These parameters formed the primary inputs for the optical, thermal, and electrical sub-models, enabling composition-resolved predictions of PV performance under dust deposition.

2.2. Optical model

The optical model quantified how deposited dust modified the spectral distribution of sunlight reaching the photovoltaic (PV) cell. It captured the effects of dust composition, particle size, and layer thickness on spectral transmittance, reflectance, and absorptance across the relevant solar spectrum. The wavelength-resolved analysis established a mechanistic link between optical attenuation and the subsequent thermal and electrical responses within the coupled framework. Therefore, the model enabled composition-sensitive assessment of wavelength-dependent losses across different dust types and mass loadings.

2.2.1. Composition-dependent optical constants

The optical modelling framework converted the measured dust chemistry into wavelength-dependent optical properties for spectral analysis. Deposited dust comprises heterogeneous mineral and carbonaceous phases, whose volume fractions and refractive behaviour control light absorption and scattering. Therefore, EDS-derived mass fractions were expressed as oxide mass fractions w_i and converted to volume fractions v_i using phase densities ρ_i, as shown in equation (1). These volume fractions were then used to estimate effective complex refractive indices over 400–900 nm, providing composition-dependent inputs for Mie scattering and radiative-transfer calculations and linking dust mineralogy to spectral and thermal effects (Novitsky et al., 2023; Zhang et al., 2011).

$$v_i = \frac{w_i/\rho_i}{\sum_j (w_j/\rho_j)}, \sum_i v_i = 1, \tag{1}$$

where w_i represents the mass fraction and ρ_i the density of oxide phase i. The use of volume fractions was important because the effective optical behaviour of a heterogeneous dust mixture depends on the volumetric contribution of each phase rather than its mass contribution alone. For each oxide or carbonaceous phase, wavelength-dependent complex refractive indices ($\tilde{m}_i(\lambda)$ of phase *i* at wavelength λ were compiled as shown in equation (2) (Rybin and Shulga, 2020). $n_i(\lambda)$ describes the phase velocity reduction while $k_i(\lambda)$ is the optical absorption.

$$\tilde{m}_i(\lambda) = n_i(\lambda) + i\, k_i(\lambda), \tag{2}$$

and the corresponding complex dielectric functions, $\varepsilon_i(\lambda)$ were calculated as;

$$\varepsilon_i(\lambda) = \tilde{m}_i^2(\lambda). \tag{3}$$

The real part of the refractive index therefore describes the phase delay of transmitted radiation, while the imaginary part represents absorptive losses within the dust phase. This distinction was important for iron oxides and carbonaceous phases, which can increase absorption in the visible region and contribute to dust-induced heating. Therefore, an effective medium approach was required to represent the combined optical behaviour of the different mineral and carbonaceous phases within the dust mixture. Both the Bruggeman and Maxwell–Garnett effective medium theories (EMTs) were considered in this study. The Bruggeman model was used as the primary approach because it is suitable for heterogeneous materials where multiple phases occur in comparable proportions without a distinct host. This allowed a statistically symmetric estimate of the effective complex dielectric function $\varepsilon_{\text{eff}}(\lambda)$ (Millán et al., 2019; Tjaden et al., 2016). The Bruggeman effective medium approximation solves equation (4) (Nayak et al., 2023; Zhang et al., 2011), while the corresponding effective refractive index and dust-layer refractive index are expressed in equations (5) and (6), respectively.

$$\sum_i v_i \frac{\varepsilon_i(\lambda)-\varepsilon_{\text{eff}}(\lambda)}{\varepsilon_i(\lambda)+2\,\varepsilon_{\text{eff}}(\lambda)} = 0 \tag{4}$$

$$\tilde{m}_{\text{eff}}(\lambda) = \sqrt{\varepsilon_{\text{eff}}(\lambda)}. \tag{5}$$

$$\tilde{m}_{\text{dust}}(\lambda) = n_{\text{eff}}(\lambda) + i\,k_{\text{eff}}(\lambda). \tag{6}$$

The Maxwell–Garnett model was applied only as a comparative sensitivity case. It assumed a host matrix with dispersed inclusions and provided a bounding estimate under contrasting microstructural assumptions (Markel, 2016). This approach was used to evaluate whether the predicted optical constants were strongly affected by the assumed internal distribution of phases, without serving as the primary model for optical calculations.

The optical constants for the dominant oxide and carbonaceous phases identified by EDS were obtained from the RefractiveIndex.info database (Polyanskiy, 2024) and compiled over 400–900 nm. However, these values represent ideal reference phases rather than direct optical measurements of the collected dust, and may not fully capture regional differences in crystallinity, impurity content, hydration state, weathering, mixed phases, and amorphous constituents. Therefore, the effective optical constants were constrained using the site-specific EDS-derived oxide fractions measured separately for Harare and Roodepoort. All refractive-index spectra were interpolated onto a common wavelength grid and lightly smoothened using a complex-preserving filter to remove numerical noise without suppressing absorption features associated with iron oxides and carbonaceous phases. This ensured that the composition-resolved dust refractive index expressed in equation (6) was evaluated consistently across the wavelength range.

2.2.2. Spectral scattering and dust-layer radiative transfer

Spectral interaction between solar radiation and the deposited dust layer was modelled using Mie theory with composition dependent refractive indices and SEM derived particle size distributions as inputs. Mie theory was selected to resolve wavelength-dependent scattering and absorption by polydisperse dust particles, allowing particle size, dust density, and mineralogical composition to be represented more realistically than in broadband attenuation models. This was important because absorbing phases such as iron oxides and carbonaceous materials can increase extinction and absorptance differently across the solar spectrum. Therefore, the Mie-based outputs were used to determine the extinction, scattering, and absorption efficiencies required for the dust-layer radiative-transfer model.

The two-stream approximation was then used to account for multiple scattering and absorption in the dust layer while maintaining computational efficiency for coupling with the thermal and electrical models. Dust was treated as a polydisperse ensemble described by a log-normal size distribution $f(r)$ characterized by mean particle radius (r_m) and geometric standard deviation (σ_g). For each wavelength and radius, Mie solutions were used to compute extinction, $Q_{\text{ext}}(\lambda, r)$, scattering, $Q_{\text{sca}}(\lambda, r)$, and absorption efficiencies, $Q_{\text{abs}}(\lambda, r)$, where

$$Q_{\text{abs}}(\lambda, r) = Q_{\text{ext}}(\lambda, r) - Q_{\text{sca}}(\lambda, r). \tag{7}$$

These efficiencies were integrated over $f(r)$ to obtain spectral mass attenuation coefficients;

$$\kappa_{\text{abs}}(\lambda) = \frac{3}{4\rho_p}\int Q_{\text{abs}}(\lambda, r)\,\frac{1}{r}\,f(r)\,dr, \tag{8}$$

$$\kappa_{\text{sca}}(\lambda) = \frac{3}{4\rho_p}\int Q_{\text{sca}}(\lambda, r)\,\frac{1}{r}\,f(r)\,dr, \tag{9}$$

where $\kappa_{\text{abs}}(\lambda)$ and $\kappa_{\text{sca}}(\lambda)$ are respectively the absorption mass attenuation coefficient and the scattering mass attenuation coefficient, and ρ_p is the effective particle density determined from oxide composition. This formalism allowed absorption and scattering contributions to be separated and weighted according to particle size and density, reflecting realistic optical behaviour of the heterogeneous dust layer. The dust layer was represented as a homogeneous absorbing-scattering slab with effective thickness, h_{eff} given by;

$$h_{\text{eff}} = \frac{M}{\rho_p(1-\epsilon)}, \tag{10}$$

where M is the measured surface mass loading and ϵ is the packing porosity. The spectral optical depth, $\tau(\lambda)$ and single-scattering albedo, $\omega_0(\lambda)$ were computed as equation (11) and (12) (Dang et al., 2019; Di Biagio et al., 2019).

$$\tau(\lambda) = [\kappa_{\text{abs}}(\lambda) + \kappa_{\text{sca}}(\lambda)]h_{\text{eff}}, \tag{11}$$

$$\omega_0(\lambda) = \frac{\kappa_{\text{sca}}(\lambda)}{\kappa_{\text{abs}}(\lambda)+\kappa_{\text{sca}}(\lambda)}. \tag{12}$$

Radiative transfer through the dust-covered interface was solved using the δ-Eddington two-stream approximation (Dang et al., 2019) to account for multiple scattering and absorption, yielding spectral transmittance $T(\lambda)$, reflectance $R(\lambda)$, and absorptance $A(\lambda)$, constrained by equation (13).

$$A(\lambda) = 1 - T(\lambda) - R(\lambda). \tag{13}$$

Angular incidence effects were incorporated using an empirical correction factor $K_\theta(\lambda)$ such that;

$$T(\lambda, \theta) = K_\theta(\lambda)\, T(\lambda), \tag{14}$$

The resulting absorptance spectrum A(λ) was then used as the radiative input for the thermal model, ensuring that composition-dependent optical losses were propagated to the predicted cell temperature. This approach captured both scattering and absorption effects for heterogeneous dust layers and provided the mechanistic link required for the coupled optical-thermal-electrical framework.

2.3. Thermal model: Conversion of absorbed radiation to heat input

Dust-layer optical absorption was translated into a spectral heat flux, which was then combined with transmitted irradiance to define the net thermal input driving the PV module, enabling iterative coupling between the dust, thermal, and electrical models. The incident plane-of-array spectral irradiance was denoted as $I_{\text{solar}}(\lambda)$, where λ is the wavelength considered over the spectral range of 400-900 nm. From the two-stream dust-layer optics, the dust layer spectral transmittance $T_d(\lambda, \theta)$ and reflectance $R_d(\lambda, \theta)$ were obtained, and the corresponding dust-layer absorptance, $A_d(\lambda, \theta)$ was defined as in equation (15) (Dang et al., 2019);

$$A_d(\lambda, \theta) = 1 - T_d(\lambda, \theta) - R_d(\lambda, \theta). \tag{15}$$

The spectral heat flux, $q''_{d,\text{abs}}(\lambda)$ absorbed within the dust layer is then given by;

$$q''_{d,\text{abs}}(\lambda) = A_d(\lambda, \theta)\, I_{\text{solar}}(\lambda), \tag{16}$$

Integration over the wavelength range yielded the total dust-absorbed radiative heat flux, which accounted for both composition- and particle-size-dependent absorption as shown in equation (17).

$$Q''_{d,\text{abs}} = \int q''_{d,\text{abs}}(\lambda)\, d\lambda = \int A_d(\lambda, \theta)\, I_{\text{solar}}(\lambda)\, d\lambda. \tag{17}$$

Radiation, $I_{\text{tr}}(\lambda)$ transmitted through the dust layer and entering the module stack is given by;

$$I_{\text{tr}}(\lambda) = T_d(\lambda, \theta)\, I_{\text{solar}}(\lambda), G_{\text{tr}} = \int I_{\text{tr}}(\lambda)\, d\lambda. \tag{18}$$

The PV module stack is optically opaque over the relevant solar spectrum, the transmitted irradiance $I_{tr}(\lambda)$ was therefore treated as being absorbed within the module stack and subsequently partitioned between (i) electrical power extracted by the PV conversion and (ii) thermalisation as heat. The extracted electrical power was taken directly from the electrical performance model shown by equation (19).

$$P''_{\text{el}} = \frac{P_{\text{max}}}{A_{\text{mod}}}, \tag{19}$$

where P_{max} is the maximum power and A_{mod} is the active PV module or solar cell area, depending on whether it is the simulation or validation case. The net heat input (Q''_{in}) driving the thermal model was therefore given as;

$$Q''_{\text{in}} = Q''_{d,\text{abs}} + G_{\text{tr}} - P''_{\text{el}}, \tag{20}$$

This formulation avoided double counting by separating heat generated within the dust layer from the absorbed transmitted component in the module stack while explicitly accounting for electrical energy removal. The convective heat-transfer coefficient (h_c) was determined based on the wind speed-dependent relationship in equation (21) where u is the wind speed in m/s and the ambient temperature was varied between 18°C and 28°C.

$$h_c = 5.7 + 3.8u \tag{21}$$

It was assumed that the top boundary of the PV module was exposed to incident solar radiation, while the bottom boundary was coupled to the ambient temperature for convective heat transfer. The sky temperature primarily influenced the top boundary through radiative heat exchange with the cooler sky, consistent with standard methodology in thermal modeling of PV systems. A one-dimensional steady-state energy balance was solved to obtain the cell temperature (T_{cell}) as shown in equation (22). The steady-state energy balance was selected because the simulations and measurements represented thermally stabilized conditions. This was preferred over a constant-temperature assumption because it allowed dust absorption and wind-dependent convection to influence the predicted cell temperature.

$$Q''_{d,\text{abs}} + G_{\text{tr}} - P''_{\text{el}} = h_c\,(T_{\text{cell}} - T_a) + \varepsilon\sigma\left(T_{\text{cell}}^4 - T_{\text{sky}}^4\right) + \frac{k_{cell}}{L_{cell}}\,(T_{\text{cell}} - T_{\text{back}}), \tag{22}$$

where h_c, T_a and ε are respectively the wind-speed-dependent convective heat-transfer coefficient, the ambient air temperature, and the effective emissivity. σ is the Stefan–Boltzmann constant while T_{sky} is the effective sky temperature. The final term represents through-thickness conduction across a cell of thickness L_{cell} and effective thermal conductivity k_{cell} to the back boundary temperature T_{back}. In the present model, T_{back} was treated as the back boundary temperature coupled to the ambient environment through the rear heat-transfer pathway. The steady-state formulation allowed the cell temperature to respond dynamically to both dust absorption and wind-dependent convection, providing a realistic thermal input for the electrical model. The resulting T_{cell} was then propagated iteratively to the electrical model to compute P''_{el}, ensuring fully consistent optical, thermal, and electrical coupling.

2.4. Electrical performance coupling

The electrical performance of the PV module was modelled using the standard single diode model, which includes the saturation current I_0, series resistance R_s, and shunt resistance R_{sh}. This model was selected to link dust modified irradiance and computed cell temperature to the main electrical outputs, including short circuit current I_{sc}, open circuit voltage V_{oc}, fill factor (FF), and maximum power P_{max}. Therefore, it was preferred over a fixed efficiency approach because it allowed the electrical response to vary with both optical attenuation and temperature rise.

The model represented the area averaged PV response under spatially averaged optical and thermal inputs. It captured reductions in current, voltage, fill factor, and maximum power caused by dust induced attenuation and heating. However, it did not resolve cell scale hotspot formation, local current mismatch, bypass diode activation, or substring level imbalance under highly non uniform dust deposition. These effects require spatially resolved electrothermal modelling supported by thermographic validation. Therefore, the present results should be interpreted as average optical, thermal, and electrical degradation, rather than a direct assessment of hotspot risk. I_0 was treated as temperature dependent and calibrated using equation (23), where E_g is the semiconductor bandgap energy, k is the Boltzmann constant, q is the elementary charge, n is the diode ideality factor, and T_{cell} is the cell temperature in Kelvin. The reference temperature was $T_{ref} = 298.15\,K$, corresponding to 25°C.

$$I_0(T_{cell}) = I_{0,ref}\left(\frac{T_{cell}}{T_{ref}}\right)^3 \exp\left[\frac{qE_g}{nk}\left(\frac{1}{T_{ref}} - \frac{1}{T_{cell}}\right)\right], \tag{23}$$

where $I_{0,ref}$ is the saturation current at the reference temperature. The current I at a given voltage V was then obtained from the single diode equation (24).

$$I = I_{ph} - I_0\left(\exp\left(\frac{q(V+IR_s)}{nkT_{cell}}\right) - 1\right) - \frac{V+IR_s}{R_{sh}}, \tag{24}$$

where I_{ph} is the light generated photocurrent and R_s accounts for ohmic losses in the cell and contacts. Since I appears on both sides of equation (24), the current voltage response was solved iteratively for each operating condition.

Electrical response was modelled by linking dust-modified spectral transmission and the computed cell temperature to I_{sc}, V_{oc}, FF, and P_{max}. The short-circuit current was computed by spectrally convolving the dust-modified transmittance with the incident spectral irradiance and the crystalline-silicon spectral responsivity as presented in equation (25).

$$I_{sc} = \int T(\lambda,\theta)\, I_{\text{solar}}(\lambda)\, SR(\lambda)\, d\lambda\,, \tag{25}$$

The open-circuit voltage was adjusted using the temperature coefficient, $\beta_{V_{oc}}$, where $T_{\text{ref}} = 25°\text{C}$.

$$V_{oc} = V_{oc,\text{ref}} + \beta_{V_{oc}} (T_{\text{cell}} - T_{\text{ref}}), \tag{26}$$

The fill factor was corrected using a temperature-sensitive single-diode formulation incorporating temperature dependence of the saturation current. The maximum power point was obtained from the current-voltage curve as shown by equation (27) and the fill factor was defined as in equation (28).

$$P_{\text{max}} = I_{sc} V_{oc} \text{FF} \tag{27}$$

$$FF = \frac{P_{max}}{I_{sc}V_{oc}} \tag{28}$$

To isolate composition-driven thermal amplification, two cases were simulated: (i) an optical-only case holding T_{cell} fixed, and (ii) a coupled optical–thermal case using the computed T_{cell}. The difference between these two cases quantified the additional power loss attributable to dust-induced heating beyond optical attenuation alone, allowing assessment of the synergistic impact of dust optical and thermal effects on PV performance.

2.5. Parametric analysis and sensitivity evaluation of the coupled framework

The coupled optical, thermal and electrical model was applied across variations in dust composition (oxide volume fractions), surface mass loading M, particle-size parameters (r_m, σ_g), surface coverage, incidence angle θ, wind speed u, and ambient temperature T_a. This parametric evaluation enabled the quantification of how each input factor influenced PV performance under realistic environmental and dust-deposition conditions. The input ranges, data sources, and modelling assumptions used in the sensitivity analysis are summarised in Table 1.

Table 1. Input parameters, ranges and sources used in the coupled optical, thermal, and electrical framework.

Input parameter	Symbol	Range used	Source
Dust mass loading	M	0 g/m² – 3.0 g/m², with 2.0 g/m² used as the representative case	Based on measured loading and the representative simulation case reported in the results
Absorber fraction	f_{abs}	0.20 – 0.72 from site dust composition	Derived from EDS oxide fractions
Particle size	r_m, σ_g	Harare: $r_m = 1.96\ \mu m$ $\sigma_g = 2.71\ \mu m$ Roodepoort: $r_m = 5.83\ \mu m$ $\sigma_g = 2.75\ \mu m$	Measured from SEM ImageJ analysis
Wind speed	u	1 – 6 m/s	Based on average location wind speed
Ambient temperature	T_a	18 – 28°C	Thermal model operating range reported in the manuscript
Incidence angle	θ	0 – 90°	Computed from solar geometry
Surface coverage	C_s	Model-derived from dust mass loading, particle size, and packing assumptions	Linked to dust mass, particle packing, and active-area obstruction

A global sensitivity analysis was performed using Latin Hypercube Sampling over the selected ranges of each input, with 1000 simulations executed using fixed random seeds to ensure reproducibility. Variance-based Sobol indices were computed from the resulting distributions of I_{sc}, V_{oc}, and P_{max}, providing a quantitative measure of the relative contribution of each input parameter to the overall variability in electrical performance. The Sobol indices were recalculated using increasing sample sizes of 250, 500, 750, and 1000 model evaluations to assess convergence. The ranking of the dominant input variables remained unchanged after 750 simulations, and the change in the main total-order indices between 750 and 1000 simulations was below 5%. This confirmed that 1000 simulations were sufficient to obtain a stable sensitivity ranking. All simulations were implemented in Python with pvlib used for solar geometry and spectral inputs. Mie scattering was computed using PyMieScatt, and spectral integration and energy-balance solvers were vectorized for computational efficiency. Input scenarios were structured using YAML configuration files, and all outputs were exported in NetCDF and CSV formats, including units, parameter definitions, and metadata for transparency and reproducibility.

2.6. Experimental validation

Experimental validation was conducted under controlled laboratory conditions to assess the reliability of the proposed optical, thermal, and electrical modelling framework. Two identical WSL C028 mono PERC crystalline silicon solar cells were used, with one cell assigned to the Roodepoort dust sample and the other to the Harare dust sample. The rated specifications of each solar cell were P_{max} = 5.5 W, V_{mp} = 5.5 V, I_{mp} = 1.0 A, V_{oc} = 6.6 V, and I_{sc} = 1.1 A under standard test conditions of 1000 W/m^2 irradiance, AM 1.5 spectrum, and 25°C cell temperature. The cell size was 185 × 185 mm, and the front surface was protected by 3.2 mm tempered glass, which represented the optical interface for dust deposition as shown in figure 2.

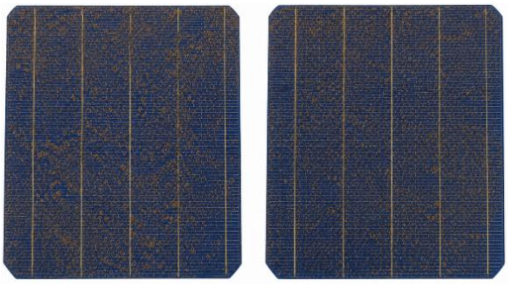

(a) (b)

Figure 2. Solar cell surfaces showing roughly uniform dust deposition patterns from (a) Roodepoort and (b) Harare.

Each solar cell was first tested under clean conditions using a calibrated solar simulator to establish the baseline electrical and thermal performance. Dust was then spread uniformly over the active surface area of each cell to obtain a dust loading of 2.0 g/m^2, to match the representative loading used in the model. The dust layer was applied as uniformly as possible to reduce local shading effects and the cells were then exposed to constant irradiance under the solar simulator and allowed to reach thermal stability before measurements were recorded.

The output voltage, current, maximum power, and cell surface temperature were measured under both clean and dust-covered conditions. The dust-induced power loss was calculated by comparing the maximum power of the dust-covered cell with the clean baseline, while the temperature rise was obtained from the difference between the measured clean and dust-covered cell temperatures. The experimental results were compared with the model predictions obtained under the same dust type, dust loading, irradiance, and ambient conditions. The percentage deviation between measured and simulated values was used to quantify the validation error for both temperature rise and power loss. Where temperature-aligned total power loss is reported, it was calculated by combining the optical-loss component with the power loss estimated from the measured temperature rise using the crystalline silicon temperature coefficient. This distinction was necessary because the validation focused mainly on confirming the dust-induced temperature rise, while the coupled framework was used to relate this thermal response to total electrical loss.

3. Results and discussions

3.1. Dust oxide composition and PSD parameters

The modelling framework was grounded on two different site compositions to represent absorber-rich and mineral-dominant dust. The resulting site-specific oxide volume fractions for Roodepoort and Harare are summarised in Table 2, while the corresponding SEM-derived particle-size distribution parameters are summarised in Table 3. These two tables define the dust-composition and particle-size inputs used to explain the site-to-site differences in spectral attenuation, dust absorption, and thermal response.

Table 2. Oxide/mineral volumetric fractions (vol%) used Bruggeman effective-medium inputs for the two site dust samples.

Component	Formula	Roodepoort (vol%)	Harare (vol%)
Silicon dioxide	SiO_2	14.9	50
Aluminium oxide	Al_2O_3	3.4	15
Iron oxide	Fe_2O_3	4.2	10
Calcium carbonate	$CaCO_3$	4.8	10
Potassium oxide	K_2O	0.8	2
Carbon (graphite)	C	67.8	10
Calcium sulphite	$CaSO_3$	4.1	3
Total		100.0	100.0

Table 3. Measured particle-size distribution parameters derived from SEM-based granulometry for Harare and Roodepoort dust samples.

Location	Scale	N	r_m (µm)	σ_g	r_{10} (µm)	r_{50} (µm)	r_{90} (µm)	$d_m = 2r_m$ (µm)
Harare	10 µm (31 px)	123	1.96	2.71	0.85	1.23	10.89	3.92
Roodepoort	20 µm (33 px)	149	5.83	2.75	1.78	4.37	25.91	11.65

The SEM-derived PSD parameters indicate clear site-to-site differences in dust fineness and dispersion. N is the number of particles and the terms r_{10}, r_{50}, and r_{90} respectively refer to the particle sizes below which 10%, 50%, and 90% of the total number of particles in a sample are smaller. Harare exhibited a distinctly finer distribution, with a median radius $r_m = 1.96$ µm, and a relatively low central tendency reflected by $r_{50} = 1.23$ µm. In contrast, Roodepoort was coarser, with $r_m = 5.83$ µm and $r_{50} = 4.37$ µm, consistent with a stronger contribution of larger particles. Despite the difference in median size, both sites showed broad, right-skewed distributions, as evidenced by similar geometric standard deviations ($\sigma_g \approx 2.7$ - 2.8) and large upper-tail percentiles. In particular, the high r_{90} values of 10.89 µm for Harare and 25.91 µm for Roodepoort confirm the presence of a non-negligible coarse fraction that can dominate surface coverage and scattering behaviour even when the median remains in the few-micron range. In operation, the finer Harare dust is more likely to form optically effective, persistent layers with greater surface area to mass and stronger short-wavelength attenuation. Conversely the coarser Roodepoort dust suggests faster gravitational settling and potentially higher resuspension thresholds, but with a coarse tail that can still drive substantial optical loss at elevated loading.

3.2. Spectral optics

The composition-resolved optical model indicated that dust layers enriched by strongly absorbing phases of graphitic carbon and iron oxides depress spectral transmittance $T(\lambda)$ predominantly in the blue-green portion of the spectrum, where the absorptive contribution is strongest. For a representative mass loading M and particle-size distribution defined by r_m and σ_g, the transmittance penalty increased toward shorter wavelengths. On the other hand, reflectance $R(\lambda)$ changes remained comparatively modest because attenuation was dominated by absorption rather than purely scattering processes. This distinction is important because it shows that the optical penalty was not only caused by light being redirected away from the module, but also by radiation being absorbed within the dust layer, which then contributed to thermal loading.

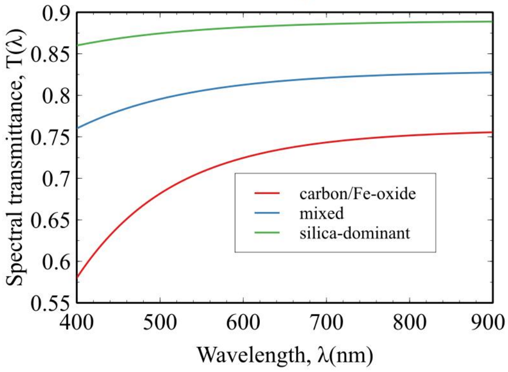

(a)

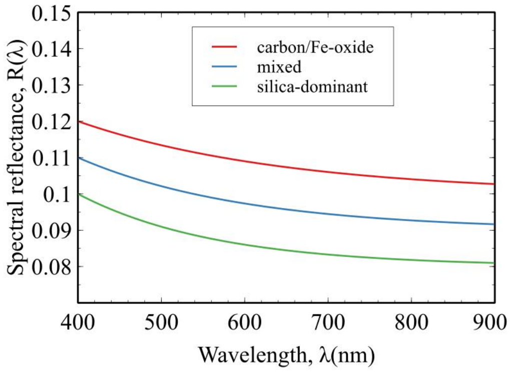

(b)

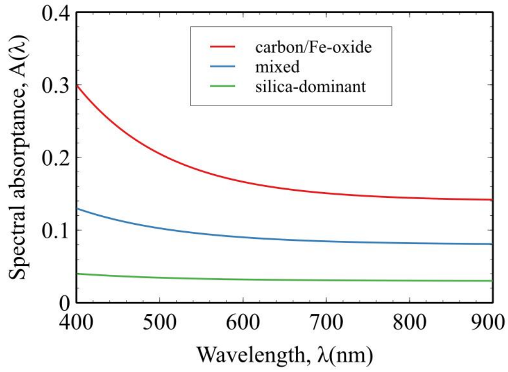

(c)

Figure 3. (a) Spectral transmittance T(λ), (b) reflectance R(λ), and (c) absorptance A(λ) for silica dominant, mixed, and carbon/Fe oxide rich dust compositions at fixed dust mass loading M, mean particle radius r_m, and incidence angle θ.

As the absorber fraction increased at fixed M, spectral absorptance $A(\lambda)$ developed a broader and higher plateau in the range of 420 - 600 nm. This confirmed that mineralogical variability governed the wavelength-selective losses rather than deposited mass alone. Therefore, Figure 3 supports the main argument of this study that dust composition, particularly the presence of carbonaceous and iron oxide phases, can control both the magnitude and spectral location of PV losses. Coarsening the PSD reflected by larger r_m reduced extinction per unit mass and flattened the spectral penalty. However, finer PSDs steepened the short-wavelength attenuation by increasing both absorption and scattering contributions. This implies that two dust layers with the same mass loading M may produce different performance losses if their particle-size distributions and absorber fractions differ. Angular effects further modulated the magnitude of loss, and oblique incidence reduced $T(\lambda)$ across the band without materially changing the spectral shape. This meant that composition remained the primary determinant of where losses occur in the spectrum. Figure 3 therefore provides the optical basis for the later thermal and electrical results, because higher $A(\lambda)$in absorber-rich dust directly increases absorbed heat input and strengthens the link between spectral attenuation, cell temperature rise, and power loss.

3.3. Absorbed heat flux and cell temperature rise

The integration of $A(\lambda)$ against the incident spectrum yielded a composition-sensitive absorbed heat flux Q''_{abs}. Absorber-rich dust increased Q''_{abs} by a factor of 1.2 - 1.6 compared to silica-dominant mixtures under clear-sky conditions. The surface energy balance converted this excess radiative input into a measurable rise in cell temperature ΔT_{cell}, and the magnitude of ΔT_{cell} was moderated by wind-driven convection and longwave exchange with the sky. This is important because Figure 4 shows that the thermal penalty was not only controlled by the amount of deposited dust, but also by the absorbing nature of the dust composition. As the absorber mass fraction increased at fixed mass loading M and wind speed u, both the normalised absorbed heat flux and the predicted temperature rise increased, confirming that mineralogy directly influenced thermal loading.

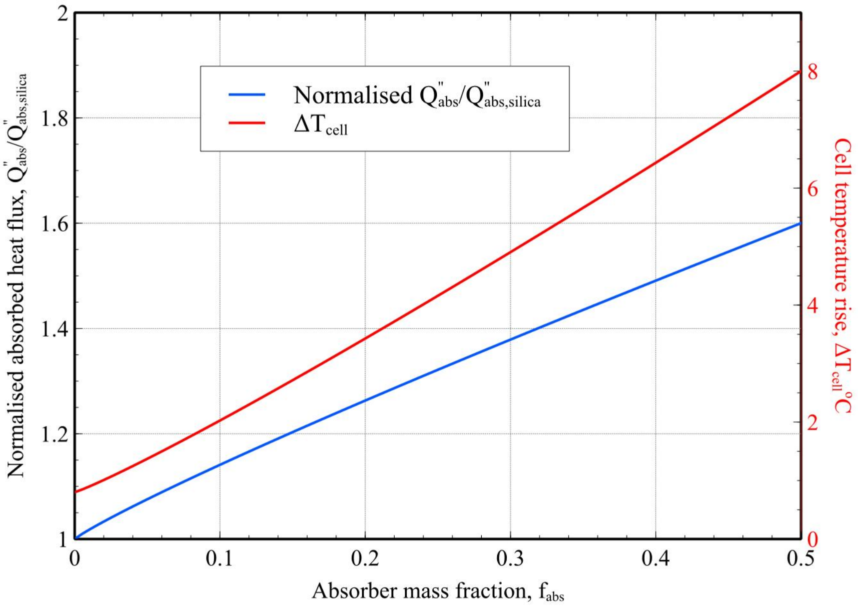

Figure 4. Normalised absorbed heat flux $Q''_{abs}/Q''_{abs,\ silica}$(left axis) and cell temperature rise ΔT_{cell}(right axis) versus absorber mass fraction f_{abs}, at fixed mass loading M and wind speed u under clear-sky mid-day conditions.

Under typical daytime ranges of irradiance and wind speed, predicted ΔT_{cell} spanned approximately 1 - 6 °C for mixed dust and reached about 8 °C for dust rich in carbon and/or iron-oxide at higher loadings within the considered range. Therefore, this indicated that thermal penalties were not constant with mass loading but increased systematically with absorber fraction and reduced convective dissipation. PSD effects were consistent with the optical trends, where finer dust increased ΔT_{cell} at the same M because higher absorptance concentrates near the front stack, while coarser dust attenuates thermal loading in parallel with its reduced spectral extinction. Thus, Figure 4 shows that composition-resolved soiling models are needed because two dust layers with similar mass loading can produce different thermal responses when their absorber fraction and PSD differ.

3.4. Electrical performance dependency on optical loss and thermal amplification

The electrical outputs reflected a photon-limited current and a temperature-limited voltage and fill factor. Optical attenuation reduced I_{sc} through the spectral overlap of $T(\lambda)$ with the crystalline-silicon spectral response and produced an approximately linear decrease in I_{sc} with the AM1.5-weighted transmittance drop. However, the dust-induced temperature rise simultaneously reduced V_{oc} and the fill factor through standard temperature coefficients. This introduced an additional composition-dependent loss beyond optical effects alone. This distinction is important because it shows that dust affected PV output through two linked pathways, namely photon loss through reduced transmission and electrical loss through increased T_{cell}. Therefore, the same optical loss did not always translate into the same P_{max} reduction when dust composition, mass loading M, and thermal conditions differed.

For further clarity, losses were decomposed into an optical-only case, computed from the dust modified spectrum while holding T_{cell} fixed, and a coupled optical thermal case using the modelled T_{cell}. The difference between these cases was treated as the thermal amplification component. Across the explored parameter space, thermal amplification increased the total power loss by approximately 20 to 60% over the optical-only estimate, with the upper range occurring under high absorber fraction, low wind speed u, and larger mass loading M. For example, cases with an optical-only loss of 9 to 10% typically increased to 12 to 16% once thermal effects were included. This was consistent with the temperature rises reported in this study and aligned with the representative case where total loss increased from 9.1% in the optical-only case to 14.2% in the coupled optical thermal case at $M = 2.0$ g/m², as shown in Figure 5. Figure 5 therefore indicates that optical attenuation alone can underestimate PV performance loss when dust contains strongly absorbing phases. Its main value is that it separates the direct spectral loss from the additional thermal penalty, making the contribution of thermal amplification clear and measurable.

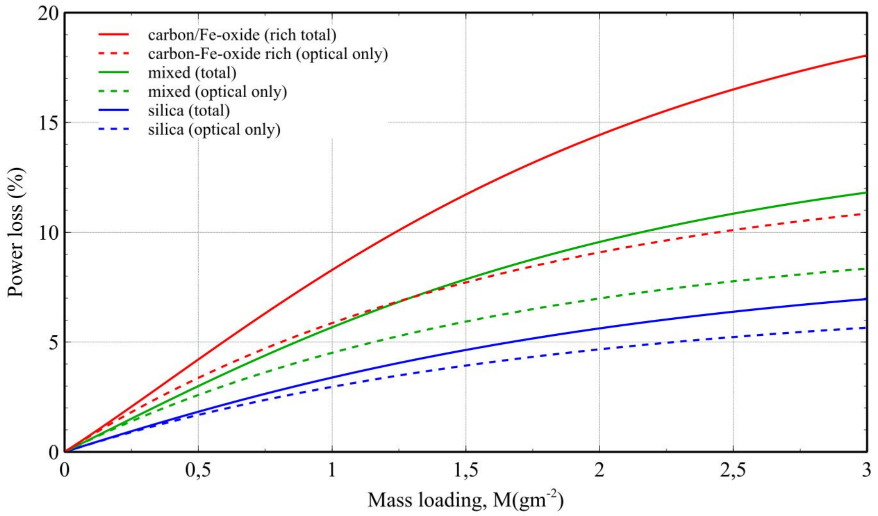

Figure 5. Loss decomposition of optical-only versus total loss across compositions and mass loadings at fixed incidence conditions and wind speed.

The experimental validation provided further support for this coupled interpretation. At the same representative dust loading of 2.0 g/m^2, the model predicted a temperature rise of 4.80°C for the Roodepoort dust case, while the measured temperature rise was 4.52°C. This gave a deviation of 5.73%. For the Harare dust case, the model predicted a temperature rise of 4.60°C, while the measured value was 4.29°C, giving a deviation of 6.81%. Using the crystalline silicon temperature coefficient of 0.45% power reduction per 1°C increase in cell temperature, the Roodepoort thermal power loss was 2.16% for the model and 2.04% for the measured case. For Harare, the corresponding values were 2.07% and 1.93%, respectively. As a result, the temperature-aligned experimental total power loss was approximately 14.08% for Roodepoort, compared with the model value of 14.20%. For Harare, the measured temperature response reduced the corresponding total power loss from 13.80% to approximately 13.66%. The small differences between the measured and predicted values indicate that the developed model reasonably captured the coupled optical, thermal, and electrical effects of dust deposition under controlled conditions.

3.5. Parametric maps and sensitivity

Two-dimensional response maps in Figure 6 represent the operational thresholds, where contours of total power loss on the plane show a rapid escalation in loss. This happens as both mass loading and absorber fraction increase and the steepening becomes pronounced when absorber fraction exceeds about 40%. Increasing wind speed shifted the loss contours upward, showing that stronger convective cooling reduced the thermal component of the power loss. Although ambient temperature was not plotted as a separate axis in Figure 6, its effect was considered in the broader parametric analysis, where higher ambient temperature increased the thermal penalty and lowered the conditions at which cleaning became necessary. This confirms that thermal amplification depends on both convective cooling capacity and the background thermal state. Figure 6 translates the coupled optical and thermal response into practical operating regions rather than only showing numerical loss trends. It shows that the same dust mass loading can produce different power losses depending on absorber fraction and wind speed, while ambient temperature further modifies the severity of the thermal penalty. Therefore, figure 6 shows that PV soiling risk cannot be assessed from deposited mass alone but must also account for dust mineralogy and local thermal conditions.

Global sensitivity analysis was conducted to quantify the relative influence of absorber fraction f_{abs}, dust mass loading M, wind speed u, particle size distribution parameters r_m and σ_g, and incidence angle θ on I_{sc}, V_{oc}, FF, and P_{max}, as shown in Figure 7. The results show that f_{abs} and M were the dominant contributors to the variability of the electrical outputs, followed by u, while PSD parameters and θ had secondary effects within the investigated parameter range. This trend is physically consistent with the coupled framework. Absorber rich dust increased spectral attenuation and absorbed heat generation, while larger M increased the optical path and active area obstruction. Wind speed mainly controlled convective heat removal and therefore affected T_{cell}, V_{oc}, FF, and P_{max} more strongly than I_{sc}. PSD effects remained relevant because finer particles increased extinction and absorption per unit mass, while incidence angle modified the angular optical path through the dust layer. Therefore, Figure 7 confirms that the main changes in PV output were governed by dust composition, deposited mass, and wind dependent thermal dissipation, rather than by optical attenuation alone. This sensitivity hierarchy also provides the basis for the cleaning trigger envelope discussed in Figure 8, where absorber rich dust, higher mass loading, fine PSDs, low wind speed, and elevated ambient temperature jointly define the conditions under which cleaning becomes more urgent.

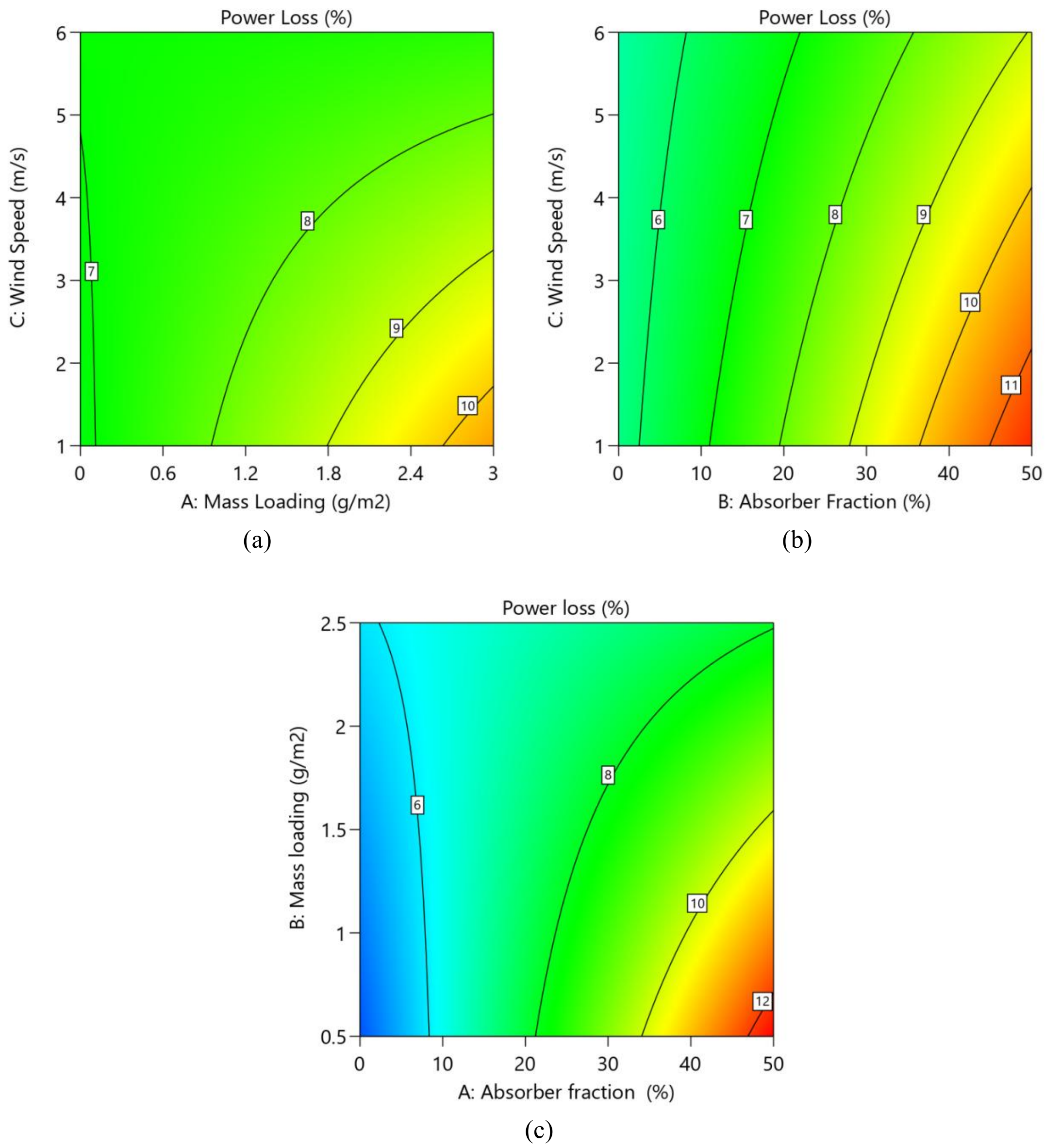

Figure 6. Contour maps of total power loss (%) showing pairwise effects of (a) mass loading M and wind speed u, (b) absorber fraction and wind speed u, and (c) absorber fraction and mass loading M, with the remaining variables held constant (ambient condition fixed).

To examine whether the use of literature derived optical constants could influence these findings, the uncertainty associated with the effective optical properties was propagated through the coupled optical, thermal, and electrical model. This was done using the variation obtained from the Bruggeman and Maxwell Garnett effective medium approximations. The propagated uncertainty was more pronounced at shorter wavelengths, where the imaginary refractive index component of iron rich and carbonaceous phases has a stronger influence on light absorption. However, within the investigated ranges, this uncertainty contributed less to the total power loss variability than absorber fraction and dust mass loading. This indicates that the main conclusions were mainly governed by the measured dust composition and deposited dust mass, although direct site-specific optical measurements would further improve the reliability of the optical parameterisation and reduce uncertainty.

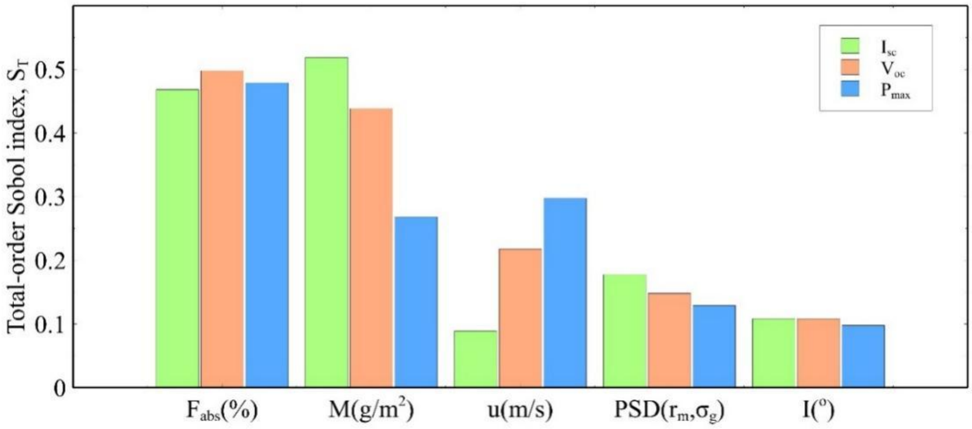

Figure 7. Global sensitivity (total-order Sobol indices) of I_{sc}, V_{oc}, and P_{max} to absorber fraction, mass loading, wind speed, PSD parameters, and incidence angle.

3.6. Operational implications

The coupled spectral–thermal framework provided actionable insights for PV system operation and maintenance. Building on the sensitivity hierarchy established in Figure 7, the analysis revealed that cleaning thresholds are mainly governed by absorber fraction f_{abs} and dust mass loading M, while wind speed u, ambient temperature, and particle-size distribution modify the magnitude of thermal amplification. This means that maintenance strategies based only on broadband transmittance or deposited mass may underestimate the cleaning requirement when the dust layer is absorber-rich, because such dust not only reduces transmitted irradiance, but also increases heat generation under high irradiance conditions. For crystalline silicon arrays operating under hot and low-wind conditions, composition-dependent cleaning triggers can mitigate an additional 3 to 5% of thermally amplified loss during peak load periods, which would otherwise be missed if only optical-only losses were considered. It is important to recognize that this operationally relevant additional loss is consistent with the upper range of thermal amplification observed across the broader parameter space, where total power loss increased by approximately 20 to 60% relative to the optical-only estimate under high absorber fraction, low wind speed, and elevated mass loading conditions. In practical terms, this translates to initiating cleaning when optical-only losses reach approximately 6 to 8% for dust layers dominated by carbonaceous or iron-oxide phases. Therefore, the proposed framework modifies maintenance decision-making most clearly in environments where absorber-rich dust coincides with high irradiance, elevated ambient temperature, fine PSDs, and weak convective cooling, conditions under which conventional optical-only approaches are likely to underestimate the true performance loss.

In contrast, predominantly silica or clay dust supports longer cleaning intervals at comparable surface mass loadings, since the temperature penalty remains modest. Particle size distribution provides an additional discriminator, because persistently fine dust particles can increase extinction and absorption per unit mass, thereby requiring tighter cleaning thresholds than coarser dust that may be more easily removed by resuspension. This means that Figure 8 is not only a summary of model outputs, but also a decision support tool for identifying when the same dust loading should lead to different maintenance actions depending on dust composition, particle characteristics, and thermal environment. The insight is practically important because it allows cleaning to be prioritized for modules exposed to high absorber fractions, fine PSDs, or both, particularly under high irradiance, elevated ambient temperature, and low wind speed.

Figure 8 translates these trends into an operating envelope for cleaning decisions by showing how absorber fraction and surface mass loading jointly define the recommended cleaning trigger band under different thermal and environmental conditions. The widening of the trigger band under low wind speed and high ambient temperature confirms that environmental conditions modify the urgency of cleaning, even when dust loading remains similar. Therefore, the study indicates that cleaning strategies should not be based only on how much dust is present, but also on what the dust is made of, how fine the particles are, and the thermal conditions under which the module operates.

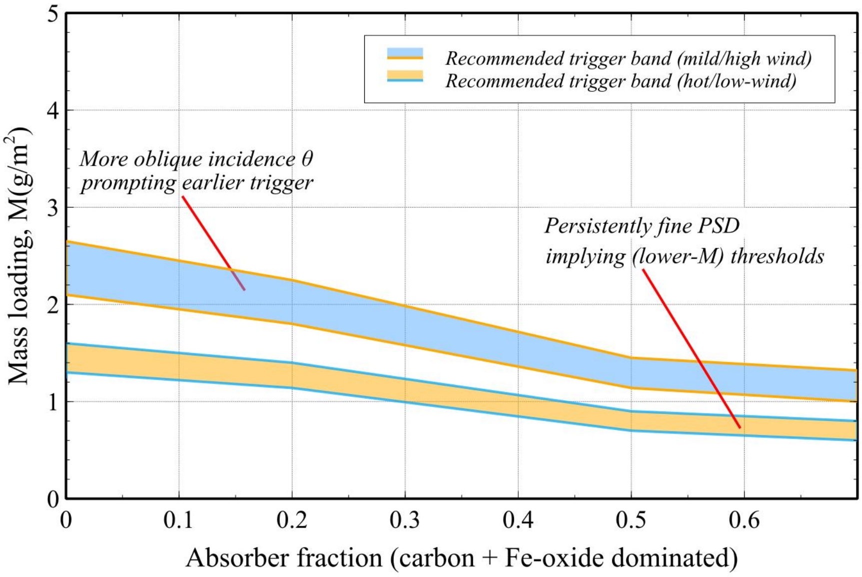

Figure 8. Operating envelope indicating recommended cleaning-trigger band as a function of absorber fraction and mass loading; the trigger band widens under low wind speed and high ambient temperature.

The framework also clarifies the type and level of input data required to implement such decision-oriented strategies in practice. Site specific measurements of dust composition, surface mass loading, and particle size distribution, together with local environmental conditions such as ambient temperature, wind speed, and solar incidence, are sufficient to parameterize the model for actionable cleaning decisions. This indicates that the framework can be applied without overly complex monitoring, since even partial characterization of these inputs can improve performance forecasting and maintenance planning compared with generic periodic cleaning schedules.

3.7. Model limitations, applicability, and future directions

Although the proposed framework was experimentally validated under controlled laboratory conditions, it is expected to perform well when the dust layer is reasonably uniform, the dust composition and particle-size distribution are representative of the deposited material, and the PV device operates under steady or near-steady thermal conditions. This is consistent with the validation procedure used in this study, where clean and dust-covered mono PERC crystalline silicon solar cells were tested under the same irradiance, dust loading, ambient conditions, and dust types used in the model.

However, the model may be less reliable under outdoor conditions where dust deposition is highly non-uniform, where particles form compacted or chemically bonded layers, or where humidity, rainfall, biological matter, and wind-driven resuspension alter the optical and thermal properties of the dust layer.

A further limitation is that cell level hotspot and mismatch effects were not explicitly evaluated. Since the model uses spatially averaged irradiance, dust loading, and cell temperature, it cannot predict local reverse biasing, bypass diode response, substring mismatch, or hotspot growth caused by patchy shading. This does not weaken the optical-thermal-electrical coupling developed in the study, but it limits the interpretation of the electrical results to average PV performance losses. Future work should combine spatial dust mapping, infrared thermography, and cell or substring resolved electrical modelling to evaluate hotspot and mismatch behaviour under non-uniform soiling.

The use of effective medium approximations and literature-based optical constants may also introduce uncertainty, particularly at shorter wavelengths where absorbing phases strongly influence spectral attenuation. In addition, the steady-state thermal formulation does not fully represent transient outdoor effects such as rapidly changing irradiance, fluctuating wind speed, precipitation, and progressive natural cleaning. Accordingly, the effective refractive indices used in this study should be interpreted as composition-resolved representative estimates rather than direct measurements of the exact mineral phases present in the local dust samples. The reliability of the framework is therefore expected to improve where the measured oxide composition closely corresponds with the reference mineral phases used to obtain the literature-based optical constants. However, higher uncertainty may arise where the local dust contains hydrated minerals, salts, organic matter, amorphous aluminosilicates, or industrial residues that are not fully represented in the available optical-constant database. Future studies should therefore include direct measurement of site-specific dust optical constants using spectral reflectance, transmittance, or ellipsometry, followed by uncertainty propagation through the optical, thermal, and electrical sub-models. This would further improve the physical realism of the optical parameterization and strengthen the predictive reliability of the coupled modelling framework.

The experimental validation performed in this study therefore supports the reliability of the coupled optical, thermal, and electrical framework under controlled and repeatable conditions. Nevertheless, future work should extend the validation to long-term outdoor PV systems using simultaneous measurements of dust loading, dust composition, particle-size distribution, module temperature, wind speed, ambient temperature, irradiance, and electrical output. This would allow further calibration under naturally evolving soiling conditions and improve the use of the framework for site-specific performance forecasting and maintenance planning.

4. Conclusion and Future Directions

The present study developed a composition-resolved optical-thermal framework that links measured dust mineralogy and particle-size distributions to wavelength-dependent optical attenuation, dust-induced heating, and electrical-performance degradation in crystalline silicon photovoltaic modules. The study derived effective complex refractive indices from oxide fractions and applied Mie-based scattering and radiative-transfer modelling coupled to a surface energy balance. The framework showed that soiling losses were not governed by deposited mass alone, because absorber-rich dust produced stronger spectral attenuation and additional thermal loading that amplified power loss beyond optical-only estimates.

Future work should prioritize field validation using concurrent measurements of spectral transmittance, module temperature, and electrical outputs under naturally evolving soiling. The model should therefore be further extended to account for non-uniform dust deposition, transient weather forcing, and cell level hotspot and mismatch effects. This can be achieved through spatially resolved electrothermal modelling, supported by infrared thermographic validation, to capture the local thermal and electrical behaviour of individual cells or substrings under realistic soiling conditions.

Declaration

AI assistance was limited to grammar editing using ChatGPT. All research analysis and content development were conducted independently by the authors.

Author Contributions

Kudzanayi Chiteka: Conceptualization, Original draft, Methodology, Investigation, Software, Formal analysis.
CC Enweremadu: Supervision, Validation, Review & editing, Formal analysis, Resources.

Funding

This research received no external funding.

Conflict of Interest Statement

The authors declare that they have no known competing financial interests or personal relationships that could have appeared to influence the work reported in this paper.

Data Availability Statement

The data that support the findings of this study are available on request from the corresponding author.

References

Abdellatif, S.O., Amr, L., Kirah, K., Ghali, H.A., 2023. Experimental Studies for Glass Light Transmission Degradation in Solar Cells Due to Dust Accumulation Using Effective Optical Scattering Parameters and Machine Learning Algorithm. IEEE Journal of Photovoltaics 13, 158–164. https://doi.org/10.1109/JPHOTOV.2022.3226711

Al Humairi, A., El Asri, H., Al Hemyari, Z.A., Jung, P., 2024. Assessing the Features of PV System's Data and the Soiling Effects on PV System's Performance Based on the Field Data. Energies 17, 4419. https://doi.org/10.3390/en17174419

Bellmann, P., Wolfertstetter, F., Conceição, R., Silva, H.G., 2020. Comparative modeling of optical soiling losses for CSP and PV energy systems. Solar Energy 197, 229–237. https://doi.org/10.1016/j.solener.2019.12.045

Boivin, L.-P., 2001. Spectral responsivity of various types of silicon photodiode at oblique incidence: comparison of measured and calculated values. Appl. Opt., AO 40, 485–491. https://doi.org/10.1364/AO.40.000485

Boyle, L., Flinchpaugh, H., Hannigan, M.P., 2015. Natural soiling of photovoltaic cover plates and the impact on transmission. Renewable Energy 77, 166–173. https://doi.org/10.1016/j.renene.2014.12.006
Dang, C., Zender, C.S., Flanner, M.G., 2019. Intercomparison and improvement of two-stream shortwave radiative transfer schemes in Earth system models for a unified treatment of cryospheric surfaces. The Cryosphere 13, 2325–2343. https://doi.org/10.5194/tc-13-2325-2019
Darwish, Z.A., Sopian, K., Fudholi, A., 2021. Reduced output of photovoltaic modules due to different types of dust particles. Journal of Cleaner Production 280, 124317. https://doi.org/10.1016/j.jclepro.2020.124317
Di Biagio, C., Formenti, P., Balkanski, Y., Caponi, L., Cazaunau, M., Pangui, E., Journet, E., Nowak, S., Andreae, M.O., Kandler, K., Saeed, T., Piketh, S., Seibert, D., Williams, E., Doussin, J.-F., 2019. Complex refractive indices and single-scattering albedo of global dust aerosols in the shortwave spectrum and relationship to size and iron content. Atmos. Chem. Phys. 19, 15503–15531. https://doi.org/10.5194/acp-19-15503-2019
Diop, D., Drame, M.S., Diallo, M., Malec, D., Mary, D., Guillot, P., 2020. Modelling of Photovoltaic Modules Optical Losses Due to Saharan Dust Deposition in Dakar, Senegal, West Africa. Smart Grid and Renewable Energy 11, 89–102. https://doi.org/10.4236/sgre.2020.117007
Drame, M.S., Diop, D., Talla, K., Diallo, M., Ngom, B.D., Nebon, B., 2021. Structural and physicochemical properties of dust collected on PV panels surfaces and their potential influence on these solar modules efficiency in Dakar, Senegal, West Africa. Scientific African 12, e00810. https://doi.org/10.1016/j.sciaf.2021.e00810
Fernández, E.F., Chemisana, D., Micheli, L., Almonacid, F., 2019. Spectral nature of soiling and its impact on multi-junction based concentrator systems. Solar Energy Materials and Solar Cells 201, 110118. https://doi.org/10.1016/j.solmat.2019.110118
Fernández-Solas, Á., Micheli, L., Almonacid, F., Fernández, E.F., 2022. Indoor validation of a multiwavelength measurement approach to estimate soiling losses in photovoltaic modules. Solar Energy 241, 584–591. https://doi.org/10.1016/j.solener.2022.06.036
Gómez, G.C., 2009. Heat transfer in a photovoltaic panel. Lund University, Lund, Sweden.
Gu, W., Wang, X., Bai, X., 2023. Coupled optical-electrical-thermal loss modelling and energy distributions of a photovoltaic module. Energy Conversion and Management 276, 116476. https://doi.org/10.1016/j.enconman.2022.116476
Hassanian, R., Riedel, M., Helgadottir, A., Yeganeh, N., Unnthorsson, R., 2022. Implicit Equation for Photovoltaic Module Temperature and Efficiency via Heat Transfer Computational Model. Thermo 2, 39–55. https://doi.org/10.3390/thermo2010004
Hoang, P., Bourdin, V., Liu, Q., Caruso, G., Archambault, V., 2014. Coupling optical and thermal models to accurately predict PV panel electricity production. Solar Energy Materials and Solar Cells 125, 325–338. https://doi.org/10.1016/j.solmat.2013.11.032
Javed, W., Guo, B., Figgis, B., Martin Pomares, L., Aïssa, B., 2020. Multi-year field assessment of seasonal variability of photovoltaic soiling and environmental factors in a desert environment. Solar Energy 211, 1392–1402. https://doi.org/10.1016/j.solener.2020.10.076
John, J.J., Rajasekar, V., Boppana, S., Chattopadhyay, S., Kottantharayil, A., TamizhMani, G., 2015. Quantification and Modeling of Spectral and Angular Losses of Naturally Soiled PV Modules. IEEE Journal of Photovoltaics 5, 1727–1734. https://doi.org/10.1109/JPHOTOV.2015.2463745
Kaneria, P., Reddy, K.S., 2025. Minimizing shadow effects to optimize solar energy input in the World Solar Challenge. Green Technology & Innovation 1, 1–18.
Kutlu, C., Erdinc, M.T., Ehtiwesh, A., Bottarelli, M., Su, Y., Riffat, S., 2025. Evaluation of operation control parameters of a residential solar organic Rankine cycle with effects of expander-generator coupling. Global Decarbonisation 1, 1–19.
Lara-Fanego, V., Gueymard, C.A., Micheli, L., 2023. Soiling Model for PV Applications: Improved Parameterizations, in: 2023 IEEE 50th Photovoltaic Specialists Conference (PVSC). Presented at the 2023 IEEE 50th Photovoltaic Specialists Conference (PVSC), pp. 1–3. https://doi.org/10.1109/PVSC48320.2023.10359694
Limane, B., Ould-Lahoucine, C., Diaf, S., 2023. Modeling and simulation of the thermal behavior and electrical performance of PV modules under different environment and operating conditions. Renewable Energy 219, 119420. https://doi.org/10.1016/j.renene.2023.119420
Lu, P., Zhang, H., Li, J., 2009. A comparison of two-stream DISORT and Eddington radiative transfer schemes in a real atmospheric profile. Journal of Quantitative Spectroscopy and Radiative Transfer 110, 129–138. https://doi.org/10.1016/j.jqsrt.2008.09.009
Mallineni, J., Yedidi, K., Shrestha, S., Knisely, B., Tatapudi, S., Kuitche, J., TamizhMani, G., 2014. Soiling losses of utility-scale PV systems in hot-dry desert climates: Results from four 4–16 years old

power plants, in: 2014 IEEE 40th Photovoltaic Specialist Conference (PVSC). Presented at the 2014 IEEE 40th Photovoltaic Specialist Conference (PVSC), pp. 3197–3200. https://doi.org/10.1109/PVSC.2014.6925615

Mandal, P., Reddy, K.S., 2025. Techno-economic assessment of solar power tower and solar parabolic dish system in India. Global Decarbonisation 1, 1–17.

Markel, V.A., 2016. Introduction to the Maxwell Garnett approximation: tutorial. J. Opt. Soc. Am. A, JOSAA 33, 1244–1256. https://doi.org/10.1364/JOSAA.33.001244

Micheli, L., Caballero, J.A., Fernandez, E.F., Smestad, G.P., Nofuentes, G., Mallick, T.K., Almonacid, F., 2019. Correlating photovoltaic soiling losses to waveband and single-value transmittance measurements. Energy 180, 376–386. https://doi.org/10.1016/j.energy.2019.05.097

Millán, C., Santonja, C., Domingo, M., Luna, R., Satorre, M.Á., 2019. An experimental test for effective medium approximations (EMAs) - Porosity determination for ices of astrophysical interest. A&A 628, A63. https://doi.org/10.1051/0004-6361/201935153

Muhfidin, R., Yu, I.-S., 2019. Thermal Analysis of PV Module and the Effect on its Efficiency, in: 2019 International Conference on Technologies and Policies in Electric Power & Energy. Presented at the 2019 International Conference on Technologies and Policies in Electric Power & Energy, pp. 1–4. https://doi.org/10.1109/IEEECONF48524.2019.9102515

Muller, M., Rashed, F., 2023. Considering the Variability of Soiling in Long-Term PV Performance Forecasting, in: Renewable Energy. Presented at the 50th IEEE Photovoltaic Specialists Conference, pp. 1–6.

Nayak, J.K., Roy Chaudhuri, P., Ratha, S., Sahoo, M.R., 2023. A comprehensive review on effective medium theories to find effective dielectric constant of composites. Journal of Electromagnetic Waves and Applications 37, 282–322. https://doi.org/10.1080/09205071.2022.2135029

Novitsky, A., Ramanovich, M., Novitsky, D.V., 2023. Operator effective medium approximation for inhomogeneous and curvilinear media. Phys. Rev. B 108, 205401. https://doi.org/10.1103/PhysRevB.108.205401

Øvrum, Ø., Marchetti, J.M., Kelesoglu, S., Marstein, E.S., 2021. Comparative Analysis of Site-Specific Soiling Losses on PV Power Production. IEEE Journal of Photovoltaics 11, 158–163. https://doi.org/10.1109/JPHOTOV.2020.3032906

Pagani, V.H., Los, N.A., Maidana, W., Leitão, P., Casaro, M.M., Nascimento, C.B., 2021. Soiling Monitoring Modelling for Photovoltaic System, in: Gonçalves, J.A., Braz-César, M., Coelho, J.P. (Eds.), CONTROLO 2020. Springer International Publishing, Cham, pp. 592–601. https://doi.org/10.1007/978-3-030-58653-9_57

Pelland, S., Pawar, P., Veeramani, A., Gustafson, W., Etringer, L.L.A., 2018. Testing Global Models of Photovoltaic Soiling Ratios Against Field Test Data Worldwide, in: 2018 IEEE 7th World Conference on Photovoltaic Energy Conversion (WCPEC) (A Joint Conference of 45th IEEE PVSC, 28th PVSEC & 34th EU PVSEC). Presented at the 2018 IEEE 7th World Conference on Photovoltaic Energy Conversion (WCPEC) (A Joint Conference of 45th IEEE PVSC, 28th PVSEC & 34th EU PVSEC), pp. 3442–3446. https://doi.org/10.1109/PVSC.2018.8548204

Perin Gasparin, F., Detzel Kipper, F., Schuck de Oliveira, F., Krenzinger, A., 2022. Assessment on the variation of temperature coefficients of photovoltaic modules with solar irradiance. Solar Energy 244, 126–133. https://doi.org/10.1016/j.solener.2022.08.052

Piedra, P.G., Llanza, L.R., Moosmüller, H., 2018. Optical losses of photovoltaic modules due to mineral dust deposition: Experimental measurements and theoretical modeling. Solar Energy 164, 160–173. https://doi.org/10.1016/j.solener.2018.02.030

Polyanskiy, M.N., 2024. Refractiveindex.info database of optical constants. Sci Data 11, 94. https://doi.org/10.1038/s41597-023-02898-2

Qaisieh, A., Abu-Nabah, B.A., Hamdan, M.O., Alami, A.H., Khanfar, L., Zaki, L., 2023. Optical characterization of accumulated dust particles and the sustainability of transmitted solar irradiance to photovoltaic cells. Renewable Energy 219, 119439. https://doi.org/10.1016/j.renene. 2023.119439

Razak, T.R., Alaoui, A.E., Jarimi, H., Ul-Saufie, A.Z., Ismail, M.H., Fuzi, M.F.M., 2026. An AI-Based Hybrid Prophet–LSTM Model for Forecasting and Financial Optimisation in Sustainable Energy Grids. Artificial Intelligence for Sustainable Cities 1, 42–60. https://doi.org/10.65582/aifsc.2026. 004

Redondo, M., Platero, C.A., Moset, A., Rodríguez, F., Donate, V., 2024. Review and Comparison of Methods for Soiling Modeling in Large Grid-Connected PV Plants. Sustainability 16, 10998. https://doi.org/10.3390/su162410998

Rezvani, M., Gholami, A., Goghsaz Ghoochani, R., Zandi, M., 2023. Review of the effect of dust characteristics on the performance of solar photovoltaic panels. Journal of Renewable and New Energies 10, 198–211. https://doi.org/10.52547/jrenew.10.1.198

Riaz, M.H., Mahmood, T., 2022. Experimental Analysis of Soiling Loss on PV Module in Cement Plant Environment. Engineering Proceedings 20, 13. https://doi.org/10.3390/engproc2022020013

Riffat, J., Samaei, S.R., 2025. Recent Advances in Perovskite–Silicon Tandem Solar Cells: Progress, Challenges, and Pathways to Commercialisation. Energy Catalyst 1, 113–126.

Rosli, M.A.M., Mat, S., Sopian, K., Sharif, M.K.A., Sulaiman, M.Y., Haw, L.C., 2014. Predicting the back surface temperature of photovoltaic modules in hot and humid climates. Jurnal Mekanikal 37, 29–36.

Rybin, O., Shulga, S., 2020. Generalized broad-band Effective Medium Theory of two-component metamaterials including magnetic ones: a review. Journal of Electromagnetic Waves and Applications 34, 1513–1549. https://doi.org/10.1080/09205071.2020.1787234

Sharma, S., Raina, G., Yadav, S., Sinha, S., 2023. A comparative evaluation of different PV soiling estimation models using experimental investigations. Energy for Sustainable Development 73, 280–291. https://doi.org/10.1016/j.esd.2023.02.008

Sisodia, A.K., 2024. Effect of dust particles size on Photovoltaic module (PV) performance. International Journal of Science and Research Archive 13, 3967–3972. https://doi.org/10.30574/ijsra.2024.13.2.2653

Smestad, G.P., Germer, T.A., Alrashidi, H., Fernández, E.F., Dey, S., Brahma, H., Sarmah, N., Ghosh, A., Sellami, N., Hassan, I.A.I., Desouky, M., Kasry, A., Pesala, B., Sundaram, S., Almonacid, F., Reddy, K.S., Mallick, T.K., Micheli, L., 2020. Modelling photovoltaic soiling losses through optical characterization. Sci Rep 10. https://doi.org/10.1038/s41598-019-56868-z

Sovetova, M., Kutlu, C., Su, Y., Riffat, S., 2025. The Potential of Small-Scale Solar Organic Rankine Cycle Systems for Decentralised Power Generation in Africa. Research and Reviews in Sustainability 1, 32–47. https://doi.org/10.5334/rss.1

Susa, M., Li, F., Nagata, K., 1992. Determination of refractive index and absorption coefficient of iron-oxide-bearing slags. Metall Trans B 23, 331–337. https://doi.org/10.1007/BF02656289

Tanesab, J., Parlevliet, D., Whale, J., Urmee, T., 2019. The effect of dust with different morphologies on the performance degradation of photovoltaic modules. Sustainable Energy Technologies and Assessments 31, 347–354. https://doi.org/10.1016/j.seta.2018.12.024

Tjaden, B., Cooper, S.J., Brett, D.J., Kramer, D., Shearing, P.R., 2016. On the origin and application of the Bruggeman correlation for analysing transport phenomena in electrochemical systems. Current Opinion in Chemical Engineering, Nanotechnology / Separation Engineering 12, 44–51. https://doi.org/10.1016/j.coche.2016.02.006

Tomšič, Š., Lipovšek, B., Bokalič, M., Topič, M., 2025. Unraveling Temperature Distribution Within Crystalline Silicon PV Modules by Different Finite Element Method-Based Thermal Modeling Approaches. Advanced Theory and Simulations 8, 2401026. https://doi.org/10.1002/adts. 202401026

Tsanakas, I. (John) A., Pilat, E., Arbaretaz, S., Doi, M.-T., Planès, E., Martins, F.M., Veludo, J., Ménézo, C., 2025. Hybrid Data-Driven Modeling and Prediction of Photovoltaic Soiling Losses: Balancing Accuracy and Simplicity. Solar RRL 9, e202500576. https://doi.org/10.1002/solr. 202500576

ul Haq, M.A., Mansur, A.A., Ghosh, S., Shamim, Md., Sheikh, Md.R.I., 2024. An Experimental Investigation of the Impact of Dust Deposition Density and Uniformity on Photovoltaic Module Output Performance, in: 2024 6th International Conference on Electrical Engineering and Information & Communication Technology (ICEEICT). Presented at the 2024 6th International Conference on Electrical Engineering and Information & Communication Technology (ICEEICT), pp. 324–328. https://doi.org/10.1109/ICEEICT62016.2024.10534536

Willers, G., Sakarapunthip, N., Ilse, K., Chuangchote, S., Gottschalg, R., 2025. Impact of Different Types of Dust on Solar Glass Transmittance and PV Module Performance. Progress in Photovoltaics 33, 844–853. https://doi.org/10.1002/pip.3930

Xu, Z., Qu, H., Li, X., Zhao, Y., Li, Y., Han, Z., 2020. Theoretical model of optical transmission and reflection characteristics of dusty PV modules. Solar Energy Materials and Solar Cells 213, 110554. https://doi.org/10.1016/j.solmat.2020.110554

Yus-Díez, J., Escribano, J., Pandolfi, M., Alastuey, A., González-Flórez, C., Gonzalez-Romero, A., Gonçalves Ageitos, M., Ivančič, M., Klose, M., Kandler, K., Obiso, V., Panta, A., Reche, C., Rigler, M., Querol, X., Perez García-Pando, C., 2025. Optical Properties and Shape-Dependent Complex Refractive Index Retrievals of Freshly Emitted Saharan Dust. EGUsphere 1–32. https://doi.org/10.5194/egusphere-2025-2571

Zarei, T., Abdolzadeh, M., 2016. Optical and thermal modeling of a tilted photovoltaic module with sand particles settled on its front surface. Energy 95, 51–66. https://doi.org/10.1016/j.energy.2015. 11.045

Zhang, D., Cherkaev, E., Lamoureux, M.P., 2011. Stieltjes representation of the 3D Bruggeman effective medium and Padé approximation. Applied Mathematics and Computation 217, 7092–7107. https://doi.org/10.1016/j.amc.2011.01.020

Zhang, Z., Gao, R., Li, Z., Wu, J., Yang, W., Liu, X., Ma, K., 2024. Experimental investigation of a monitoring model for dust deposition on solar photovoltaic modules. International Journal of Green Energy 21, 625–639. https://doi.org/10.1080/15435075.2023.2202739